Genesis and Evolution of Hierarchical Cloud Clusters in a Two-Dimensional Cumulus-Resolving Model

L. PENG

Space Applications Corporation, Vienna, Virginia

C.-H. SUI, K.-M. LAU, AND W.-K. TAO

Laboratory for Atmospheres, NASA Goddard Space Flight Center, Greenbelt, Maryland

(Manuscript received 27 July 1998, in final form 3 August 2000)

ABSTRACT

A two-dimensional cloud ensemble model is integrated over a basin-scale domain with prescribed sea surface temperature (SST), to study the formation and evolution of cloud clusters over a large-scale warm pool. Neither a basic zonal flow is prescribed nor is a single perturbation initially given. The results show that deep convective clouds appear in hierarchical clustered patterns and are limited to the area of warm SST above 28°C. The most fundamental cloud cluster in the model has a horizontal scale of a few hundred kilometers, in which new cumulus clouds are generated at the leading edge of a propagating surface cold-air pool—the ''gust front.'' It may last for days and propagate for a long distance if the background flow is broad and persistent as is the case in the low-level convergence zone of the SST-induced background flow.

The largest hierarchical propagating cloud systems in the model have horizontal scales up to 3000 km and consist of up to four cloud clusters that are generally of gust front type. The constituent cloud clusters are generated intermittently and have life spans of 12–36 h. The internal heating of the constituent clusters collectively induces an overall troposphere-deep gravity wave. The overall wave travels in the direction of the tropospheric deep shear at a speed determined by the thermodynamic asymmetry in the wave created by the transition from warm and moist incoming air in the front to drier and cooler air in the rear.

The development of new cumulus clusters in the front region of the hierarchical system is due to the combined effect of the overall wave and the gravity waves excited by the constituent clusters on the lower-tropospheric stability. When there are no interruptions from outside the cloud system, new cloud clusters developed intermittently from shallow disturbances hundreds of kilometers ahead of the existing deep convection. The resulting hierarchical cloud pattern resembles the observed equatorial super cloud cluster (SCC) in the time–longitude diagram. However, the life spans of the constituent clusters of the system are shorter than that in the observed SCC.

1. Introduction

Tropical deep convective systems as revealed by satellite images are clustered in multiple time- and space scales (Nakazawa 1988; Yano and Nishi 1989; Lau et al. 1991; Sui and Lau 1992; Mapes and Houze 1993; Chen and Houze 1996; and others). One of the most intriguing features is the large-scale traveling hierarchical cloud pattern known as a super cloud cluster (SCC) in which individual cloud clusters (CCs) propagate mostly against the traveling of the overall envelope (see, e.g., Nakazawa 1988). The search for mechanisms responsible for the hierarchical structures and movements has been a major research topic in tropical climate dynamics in the past decade.

Several mechanistic numerical models (Lau et al. 1989; Chao and Lin 1994; Yano et al. 1995; Chao and Deng 1998) and aqua-planet general circulation models (Numaguti and Hayashi 1991; Kuma 1994) have been used to simulate the hierarchical cloud patterns. In a 5-level global model, Lau et al. (1989) found SCC-type disturbances evolving from random initial conditions near the equator. Yano et al. (1995) also obtained SCC-like hierarchical cloud patterns from random initial conditions in their equatorial beta-plane shallow-water-equation model with certain cloud parameterization. Those results imply that a mechanism or mechanisms favoring the hierarchical patterns exist in the beta-plane or global models. Moreover, Chao and Lin (1994, hereafter referred to as CL), by starting from a single, instead of random, perturbation, obtained SCC-like hierarchical cloud patterns in a longitude–height two-dimensional

Corresponding author address: Dr. C.-H. Sui, Laboratory for Atmospheres, NASA Goddard Space Flight Center, Mail Code 913, Greenbelt, MD 20771.
E-mail: sui@climate.gsfc.nasa.gov

(2D) hydrostatic model with a prescribed nonzero easterly zonal mean flow. They demonstrated what they called a ''tele-induction mechanism.'' Namely, in the mature phase of an existing cloud cluster, a CC-scale downdraft forces the boundary layer air to move eastward on the east side of the cloud and creates a boundary layer convergence that initiates a new cloud cluster to the east of the existing one. The successive generation of new cloud clusters in the east and the subsequent decay of existing ones give rise to an eastward-moving SCC. In the model of CL, the two most critical elements, beside gravity wave dynamics, are the selected cumulus parameterization scheme and the externally maintained (prescribed) nonzero zonal-mean flow. The latter biases the otherwise isotropic dynamics toward favoring the SCC-like mode. Without it, there would be no SCC-like hierarchical cloud patterns in CL (see Chao and Deng 1998). The former is critical to the SCC-like pattern not only in CL but even more so in 3D models (Chao and Deng 1998).

It should be noted that the prescribed nonzero zonal-mean flow in a longitude–height 2D model is only an expedient. It seems unlikely that the process maintains the zonal mean flow yet never significantly affects nor interacts with the clustering processes. Of course, the most natural but uneconomical choice is a beta-plane or global model with the earth's rotation that introduces anisotropic modes into the otherwise isotropic dynamics and is capable of maintaining zonal-mean flow at the equator. One may also wonder whether the scale of the overall cloud pattern will be the same if the model starts from a white noise instead of a single perturbation. Above all, using a cumulus-parameterized model to investigate the mechanism of hierarchical cumulus pattern is an unsound approach that leaves the results in doubt. To avoid the uncertainty and controversy inherited in cumulus parameterization, further studies on hierarchical cloud pattern should at least adopt a cumulus-resolving model.

Beside the cumulus-parameterized model studies, Mapes (1993) showed that the phase-speed difference between the two deepest internal gravity waves, as generated by an intense cumulus convection, can induce low-level convergence between the wave fronts and may set up distant new convection. Note, however, that repeated actions of such a mechanism would tend to generate a very noisy cloud field unless being constrained or regulated by other mechanisms and/or large-scale environmental factors.

Here is the most fundamental question: Is clustering an intrinsic property of deep moist convection? In other words, can moist convection organize in clusters under horizontally uniform environment? This question was investigated by Nakajima and Matsuno (1988) using a 2D cloud-resolving model over a 512-km domain under horizontally uniform conditions. Among the experiments they carried out, ''double-scale'' structures (i.e., cloud clusters) were indeed found in the experiments that included cloud microphysics, specifically the evaporation of raindrops. So the answer to the above question is affirmative. Based on the model results, the principal mechanism for the generation of the cloud cluster is the formation of a cold-air pool at the foot of each deep cloud due mainly to the evaporation of rain water. The cold-air pool limits the lifetime of the existing individual cloud cell and, at the same time, spreads out in the form of a density current and triggers new cloud at the edges of the pool. Several clusters are found 50 to 200 km apart scattered over the model domain. They meander in individual paths in an x–t diagram with no common direction, thus bearing no resemblance to the observed SCC. Although the large-scale part of the results needs further confirmation with a much larger domain, it seems certain that including a prescribed nonzero zonal mean flow (or the beta effect if in 3D), or introducing a large-scale horizontally nonuniform environment, or simply starting from a large-scale finite initial disturbance would likely help to organize the clusters into a higher-level structure.[1]

In the equatorial region where SCCs are found, horizontal nonuniformity almost always exists. The higher sea surface temperature (SST) in the Pacific warm pool is one obvious example. Can such a large-scale SST nonuniformity (and its induced Walker-type cells) help the genesis, development, and maintenance of hierarchical cloud clusters, particularly the SCC type, with no need of prescribing a nonzero zonal mean flow nor starting from a large-scale single perturbation? It is reasonable to expect that the Walker-type circulation associated with the SST nonuniformity would provide favorable environment for hierarchical cumulus patterns to form, that the grand scale of the patterns would generally depend on the horizontal dimension of the SST nonuniformity, and that the evolution of the overall system would depend upon the interactions between the multiple spatial and temporal scales spanned by the individual cumulus convection and the slowly varying Walker cells. A study of such a system would contribute to our understanding of hierarchical cloud organizations as well as tropical cumulus dynamics in general.

With such expectations, we integrate a 2D cumulus-resolving model over a large all-ocean area with prescribed idealized SST distribution of warm-pool type (referred to as WP hereafter), to investigate the hierarchical cloud structures in the system and the possible effects of the SST nonuniformity on their formation and evolution. As a first step, the earth's rotation is neglected. The model and the experiment are described briefly in section 2. After an overview of the results in section 3, we first

[1] During the review process of this paper, a paper by K. Oohchi appeared in *J. Meteor. Soc. Japan* (Oohchi 1999). SCC-like hierarchical cloud organizations were successfully developed from an initial large-scale eastward-moving gravity wave in a 2D cumulus-resolving model in which a basic easterly zonal flow is prescribed.

describe in section 4 the stationary and quasi-steady flow induced by the prescribed SST gradient, then discuss the gust front–type cloud clusters in section 5 and the cloud patterns of higher hierarchy in section 6, followed by a summary and some remarks in section 7.

2. The numerical experiment

Beside the difference in horizontal domain size, the model is essentially the 2D version of the Goddard Cumulus Ensemble Model (GCEM) with one basic modification; namely, the original Wilhelmson–Ogura anelastic approximation is replaced by the energy conserving Lipps–Hemler anelastic approximation (Lipps 1990; Bannon 1995). The GCEM was originally based on the model developed by Soong and Ogura (1980), Soong and Tao (1980), Tao (1983), and Tao and Soong (1986). The full formulations, including later improvements, are described in Tao and Simpson (1993). The model's cloud microphysics include a parameterized Kessler-type 2-category (cloud water and rain) liquid water scheme and a parameterized Lin et al. (1983) 3-category (cloud ice, snow, and hail/graupel) ice-phase schemes. The saturation adjustment scheme for removing supersaturated vapor or removing subsaturation in the presence of cloud is described by Tao et al. (1989). The subgrid-scale turbulence in the model is based on Deardorff (1975), Klemp and Wilhelmson (1978), and Soong and Ogura (1980). A prognostic equation is solved for subgrid kinetic energy that is then used to specify the eddy coefficients. Heat and moisture fluxes at the sea surface are obtained from bulk formulation. The model has 31 vertically stretched levels with the top at 21 km. Rayleigh damping with coefficient increasing with height is used above 16 km to reduce upper-boundary reflection.

In this experiment, the horizontal domain is covered by 6144 grid points with 2.5-km separation (total 15 360 km) plus 50 grid points on each side stretching outward toward the open lateral boundary with 1.05 stretching ratio. The open lateral boundary condition follows that of Klemp and Wilhelmson (1978). Because of the use of a stretched horizontal grid the model will be less sensitive to the choice of gravity wave speed associated with the open lateral boundary condition (Fovell and Ogura 1988). The lower boundary is all ocean. The SST is prescribed and held constant in time. The prescribed SST distribution is domain symmetrical, 26°C over the stretching grids, 29.5°C over the central area of 6670 km wide (between grid 1790 and grid 4457), and linearly interpolated values in between (see Fig. 4e). The SST distribution serves two purposes: to represent an idealized WP where cloud development and propagation can be investigated, and to keep cloud development away from the lateral boundary. The initial condition is an atmosphere at rest with zonally uniform thermodynamic properties. The vertical profiles of temperature and humidity are the averaged values over the Tropical Ocean Global Atmosphere (TOGA) region over the periods when convective activities are relatively suppressed. Figure 1 shows the temperature and dewpoint temperature in a skew-T–log$P$ diagram. No clouds are present initially. The integration is carried out for 27 days. Treated as merely an overall dissipation mechanism, radiation is computed using the mean solar zenith angle and zonal mean temperature and humidity profiles.

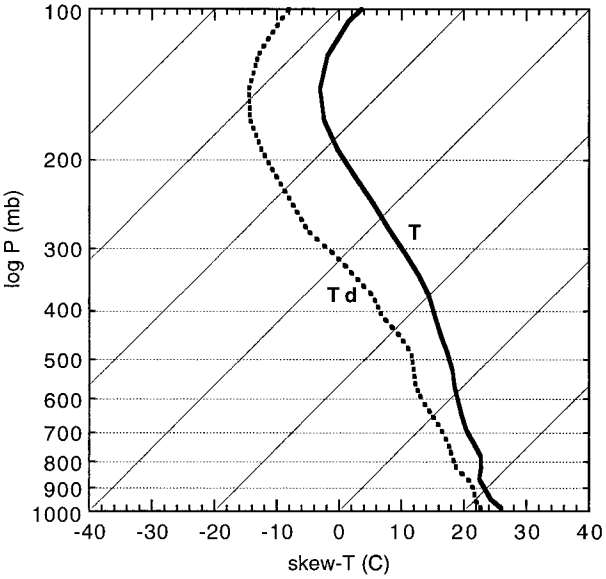

FIG. 1. Initial temperature T and dewpoint temperature Td.

The adopted initial atmosphere is conditionally unstable below 1.4 km and between 1.8 and 4.8 km. The stable layer between 1.4 and 1.8 km reflects the fact that the profile is taken from a period in which shallow clouds usually prevail. For an air parcel lifted from the lowest level (173 m), the level of free convection estimated by the parcel method is between the second (536 m) and the third (922 m) grid levels and the top of positive buoyancy is about 11 km. The estimated convective available potential energy (CAPE) of the parcel is just about 320 J kg^{-1}. The estimated work done to lift the parcel through the layer of negative buoyancy, requisite for the CAPE release, is about 50 J kg^{-1}. Since the parcel method underestimates the work requirement for deep convection, more work done is required to actually bring an air parcel up to the second conditionally unstable layer in order to start free deep convection. The lifting requirement for deep convection gives any existing meso- or large-scale system a chance to influence the cumulus organization and its evolution by providing the required lifting.

3. An overview

Before describing the results, it is noted that there is large disequilibrium between the imposed SST gradient and the initial zonally uniform atmosphere. This dis-

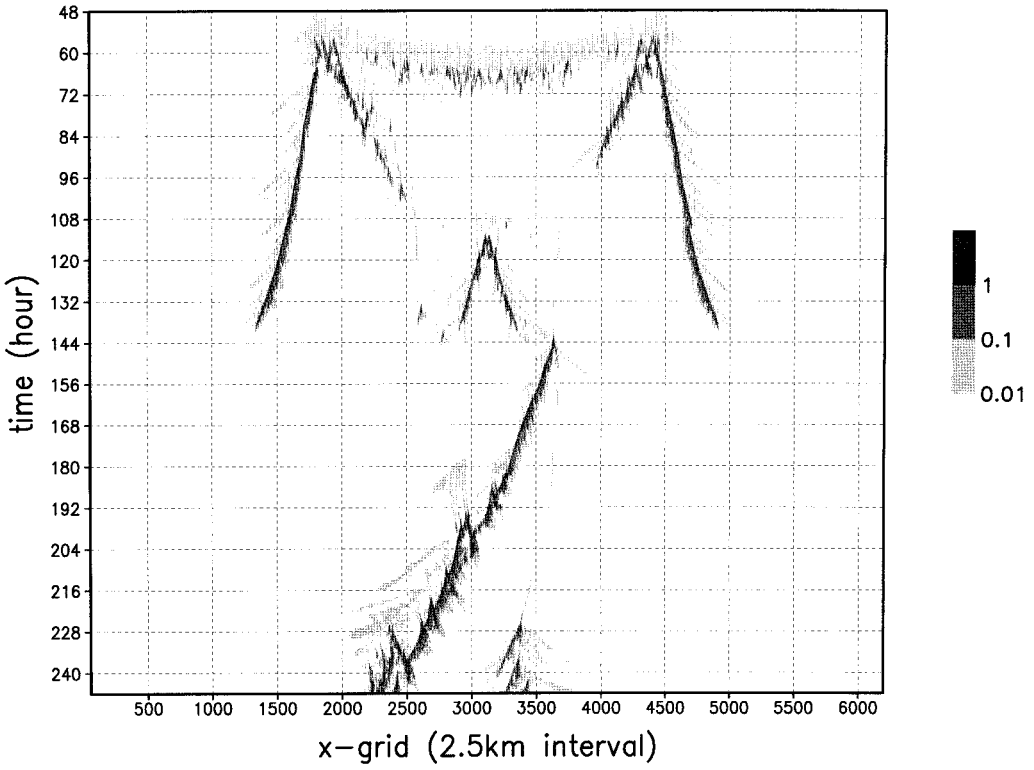

FIG. 2. An x–t diagram of cloud content q_c (sum of mixing ratio of all water and ice cloud species, unit g kg^{-1}) at 1.33 km. Grades of shade: 0.01, 0.1, 1.

equilibrium artificially imposes a large-scale pattern on lower-boundary forcing and therefore the initial large-scale developments in the experiment are artifacts and should be looked upon as merely spinup processes. The smaller-scale processes are nevertheless still informative.

Figure 2, the time–longitude section of the cloud content (the total mixing ratio of all water and ice cloud species) at 1.33 km, outlines the convection between model hour 48 and 246. One notices that the so far well-preserved domain symmetry abruptly breaks down at hour 144 when all the convection activities nearly vanish. It is simply due to numerical error accumulation. The numerical scheme for solving the elliptic perturbation-pressure equation does not preserve domain symmetry. The asymmetry emerges at the time of the weakest fields, which are presumably most vulnerable to error.

Cumulus onset occurs at the beginning of the third day near the edges of the WP. The cloud area immediately spreads out in both directions, but the clouds remain shallow for 6 to 12 h until some of the convective cells finally penetrate the stable layer between 1.4 and 1.8 km and grow into precipitating deep convective storms.

After the initiation of deep cumulus clouds, two large cloud systems develop near the two edges of the WP, respectively, then split into four. Two move outward and the other two move inward. These and other cloud systems completely vanish around hour 144. A new cluster appears now near the domain center, propagating westward. Seventy-five hours later another one appears but moves eastward. The subsequent evolution can be seen in Fig. 3, the time–longitude section of the cloud content at 6 km. The two clusters continue their outward propagation until vanish over the cooler water. Before then, a new cluster appears near the domain center and splits, going in opposite ways. Figure 3 further shows the following.

1) Cumuli in this experiment generally appear as organized and propagating clusters that last up to several days. The properties of the most frequent ones will be presented and discussed in section 5.
2) Between hours 456 and 588, a large-scale cluster propagates steadily across the WP from the left edge to the right edge. It will be discussed in details in section 6.
3) Around hour 482, several deep cumulus clouds appear over the WP between the two newly developed eastward-moving clusters but disappear in less than a day. The reason is discussed in section 5.
4) The suppression of deep convection over the cool water is evident. SST seemingly also affects the propagation and compactness of a cloud pattern. The two widely separated clusters shown in the top part

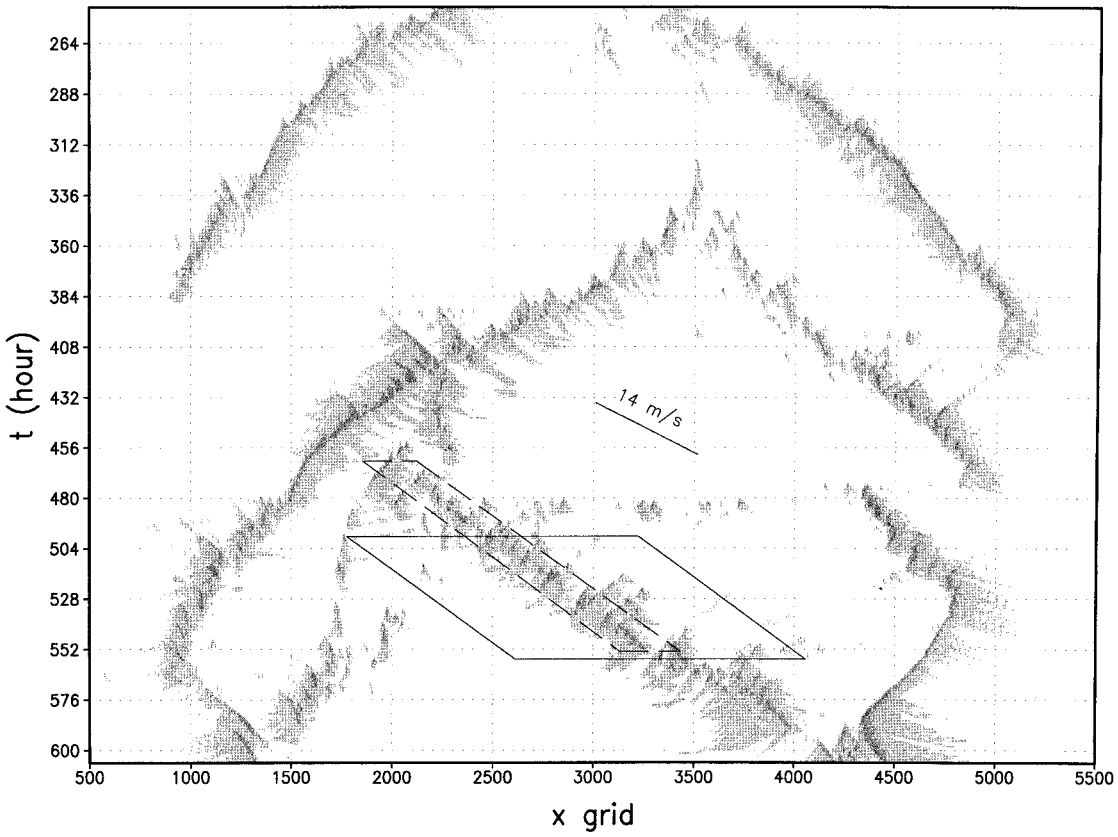

FIG. 3. An x–t diagram of cloud content (g kg^{-1}) at 6 km. Grades of shade: 0.02, 1.

of Fig. 3 slow down after crossing the edge of the WP (see the appearance of inward turning). The slowing down is accompanied by a change of clustering to a more compact or denser structure (see, e.g., from hour 264 to hour 312 on the left and from hour 288 to hour 336 on the right). The two cloud clusters that cross the central region clearly travel faster than any of the cluster outside or near the edge of the WP and are the least compact. Moreover, when entering the cold water area too far, a cloud pattern either dissipates or reverses the direction of propagation. It is noted that when the atmosphere is more humid over the cool water in the later stage of the experiment, the clusters of deep convective clouds off the warm water no longer completely vanish but only shift around.

4. The large-scale flow induced by the prescribed SST gradient

Through the lower boundary fluxes the imposed SST gradient would induce a large-scale flow of its own if there were no other sources of variability in the model. In the presence of other sources of variability the imposed SST gradient is still capable of impose its own scale on the model as one of its spectral component in the long run. A discussion of the effects of the imposed SST gradient on the model's variability should include the effects of the SST-induced flow too, not just the instantaneous effects of the surface fluxes.

The total flow after the onset of deep convection is locally dominated by deep cumulus cells and further complicated by the formation of mesoscale and large-scale convection clusters. Averaging over suitable time intervals can nevertheless expose the stationary or slow-changing features. Figure 4a shows the mean zonal wind distribution over the 6-day period between hours 462 and 606. The mean winds are inward toward the center below 6 km and outward above. The inflow decreases from the boundary layer up and the level of maximum outflow is around 13 km. Both the maximum inflow and outflow are approximately located above the midpoint of the area of nonuniform SST (see Fig. 4e), which means that the vertical line passing through this point approximately separates ascending from descending motion and horizontal divergence from horizontal convergence. These features are consistent with the imposed SST gradient except that the right-hand side circulation is significantly stronger than the one on the left-hand side. Since the prescribed SST is symmetric about the center and the other model parameters and the initial conditions are horizontally uniform, the circulation directly forced by the SST gradient is expected to be

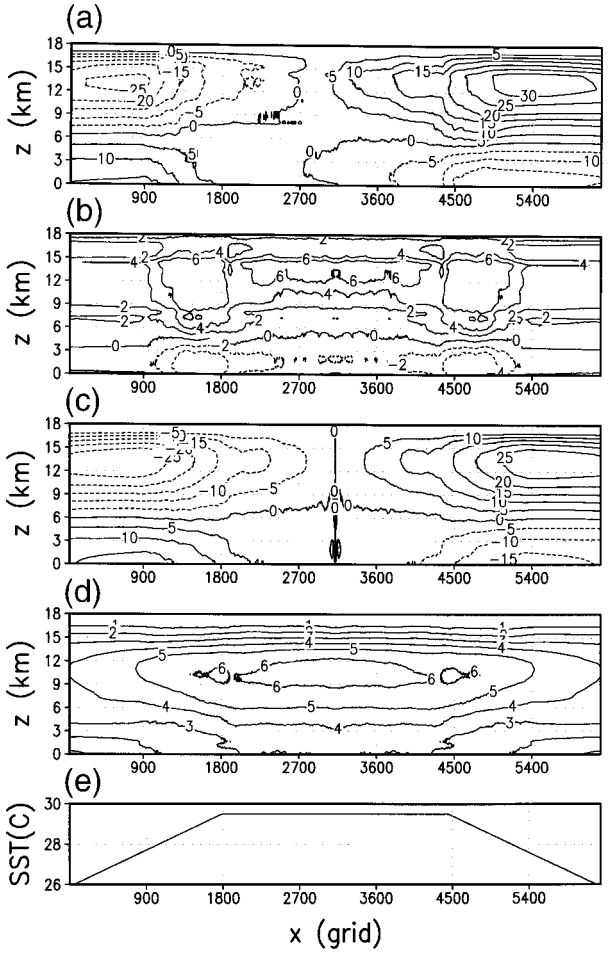

FIG. 4. Mean variables between hours 462 and 606. (a) Zonal wind u (m s^{-1}); (b) antisymmetric part of u; (c) symmetric part of u; (d) temperature deviation from the initial condition, symmetric part only (°C); (e) prescribed SST (°C).

symmetric about the central vertical line. The symmetric component of the mean flow is shown in Fig. 4c after being separated from the antisymmetric component. A very similar symmetric mean flow field is obtained in the 6-day period from hour 318 to hour 462 except about 5 m s^{-1} weaker in maximum wind. Therefore, the symmetric flow pattern in Fig. 4c well represents the SST-induced slowly varying stationary circulation in the model. It is referred to hereafter as the SST-induced large-scale flow. One notices that the strongest low-level convergence in the symmetric flow is located almost directly above the location of the sharpest reduction of SST gradient in the flow direction, that is, the edge of the uniform SST. Figure 4d shows the mean symmetric field of temperature deviation from the initial condition in the same time period, which is generally similar to the mean symmetric buoyancy field. It is noted that the forced circulation and warming shown in Fig. 4 are stronger than expected and the resulted increase in static stability in the lower atmosphere tends to suppress cumulus activity. The warming and forced circulation would be reduced if radiation computation were not simplified and, perhaps more importantly, if the effects of Hadley circulation were included. In addition, the simple radiation lateral boundary condition may also share some blame. Note in passing that the antisymmetric mean flow (Fig. 4b), likely a product of nonlinear interaction, is westward below 4 km and eastward above. It is almost zonally uniform over the WP. As mentioned in the previous section (see Fig. 4), in the same 6-day time period there is a large-scale cloud cluster propagating eastward across the WP from one side to the other. The antisymmetric mean flow over the WP is apparently related to the moving cloud cluster.

5. Cloud clusters associated with the gust front

Under the convective cloud that rains, there is a subcloud layer colder than the surrounding due to the evaporation of falling raindrops. Depending on the depth of the layer and the sharpness of temperature gradient at its edge, the cold layer may move as a density current. When it does, it generates a system of clouds, which may be called the ''gust front''–type cloud system. This is the fundamental and most frequent cloud cluster in the model. The two outer clusters in hours 270–384, the cluster on the left side in hours 444–480, the four early clusters in hours 66–140, the central cluster in hours 144–186, and many others fall into this type. Density currents and squall lines have been extensively studied analytically and numerically (e.g., Moncrieff and Miller 1976; Rotunno et al. 1988; Fovell and Ogura 1988; Moncrieff 1989; Xu and Moncrieff 1994; Chen 1995; Fovell and Dailey 1995; Liu and Moncrieff 1996; Yang and Houze 1995; Xue et al. 1997; Lin et al. 1998; Moncrieff and Liu 1999). In this model, unlike the models with a controlled environment, the thermodynamic and wind profiles are spatially nonuniform and varying with time. In the following, we shall focus on the effects of variable environment on the cloud clusters related to the gravity currents.

In the gust front cloud system, the cold air behind the front pushes forward while the air in front of it is forced to climb up the front edge and flow atop the surface cold layer. The strongest updraft is mostly at the front edge. The cloud cells and gravity waves generated by the updraft at the front edge travel backward relative to the front. These common features are most clearly seen in Fig. 5, the 24-h moving composite of the cloud cluster on the left side of the uniform SST between hour 294 and hour 318. The moving reference point for the composites is the gust front. A moving composite is also made for the right-side cloud cluster in the same period (not shown). The two cloud systems are moving outward relative to the center of the uniform SST at speeds 6 and 9 m s^{-1}, respectively (see Fig. 3). With respect to their moving directions, the distributions of cloud, velocities, and temperature in the two composites

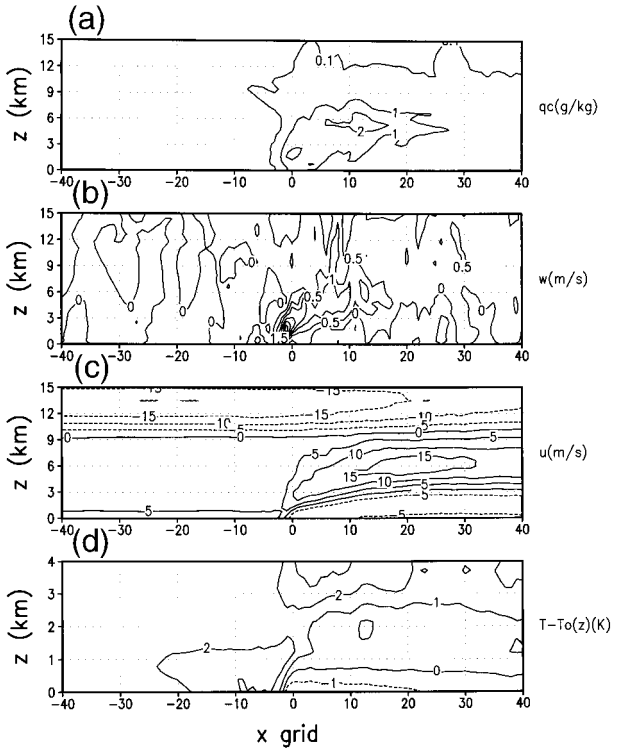

FIG. 5. Composite fields of the left-side cloud cluster between hours 294 and 318. (a) Cloud content q_c, (b) vertical velocity w, (c) zonal velocity u, and (d) temperature deviation from the initial condition.

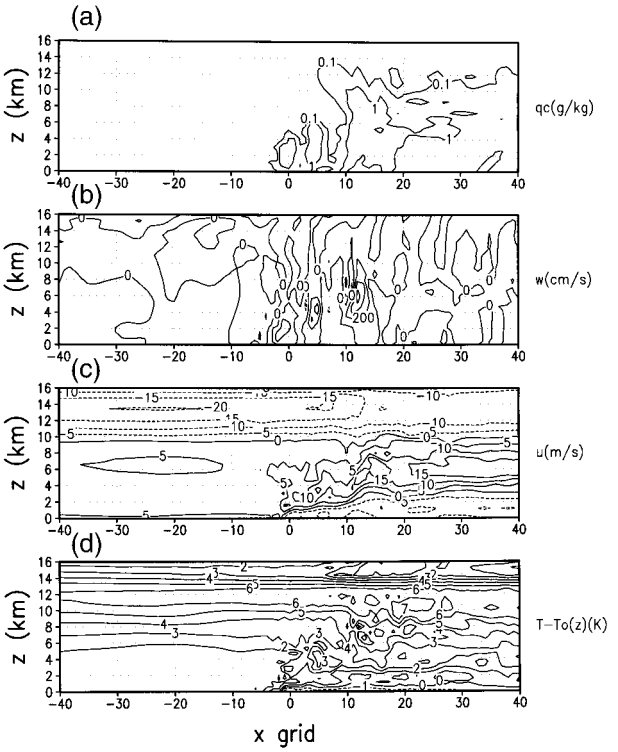

FIG. 6. Snapshots of the left-side cloud cluster at hour 306. (a) Cloud content q_c, (b) vertical velocity w, (c) zonal velocity u, and (d) temperature deviation from the initial condition.

are qualitatively quite symmetric. In each case, a surface cool-air pool is clearly evident up to 1 km or higher, with stronger temperature gradient at the front. A deep layer of light wind with little shear blows toward the front. After being pushed up at the front by the opposite cool surface winds, the climbing-over winds become confluent and speed up on top of the cool-air layer. The upward motion at the front induces divergence in the upper troposphere where the large-scale or background flow is in the direction of the surface cool wind and the propagation of the system.

The composite properties shown in Fig. 5 very well depict the overall structure of the convection of this type but miss the multiple-cell details of the convection, which move relatively to the gust front and hence have been mostly canceled out by averaging. Figure 6 is an instant snapshot at hour 306 of the cloud system near the left edge of the uniform SST. The surface cold-air pool and other characteristics seen in the composites are evidently all here. More revealing are the multiple cells above the cool-air pool with dominant horizontal scale 15–20 km. Three cells appear rearward one after another and the fourth one has become much weak but still recognizable. The cloud systems of this type are similar in structure to the multiple-cell storms simulated by several 2D models with specially selected wind shears. The multiple-cell structures there have been discussed in the literature and several mechanisms have been suggested (see Fovell and Ogura 1988; Yang and Houze 1995; Lin et al. 1998).

To understand the genesis of this type of cloud systems in the model, it is instructive to examine the formation of the surface cold-air pool and its interaction with the background or mesoscale winds. Figure 7 shows that a deep cumulus cloud has been well developed over the grid points 3627–3636 by hour 143. Below 3 km, there is an asymmetric mesoscale flow with respect to the cumulus cell. On its left, the wind is toward the cloud area with maximum speed about 8 m s^{-1} while on the right side the wind is practically calm. To see the effect of the flow asymmetry, boundary layer mean zonal wind (dashed) and mean perturbation temperature (deviation from the initial state, solid line) are plotted in Fig. 8 at selected hours 144, 145, 146, and 150, respectively. The flow streamlines in the vertical plane are also shown in Fig. 9 for the selected hours 144, 145, and 146. By hour 144, a cold-air pool of ~0.5 km deep and ~25 km wide has formed under the cumulus cloud. Once the cold-air pool exists, it moves with the flow toward the right. This generates strong updrafts on the right and in the center, further enhances the convection and the temperature gradient, and expands the cold-air pool. At hour 145, a strong cold downdraft is generated and split in both directions near the surface. The cold-air outflow on the left meets the preexisting warmer flow head-on and begins to shift the

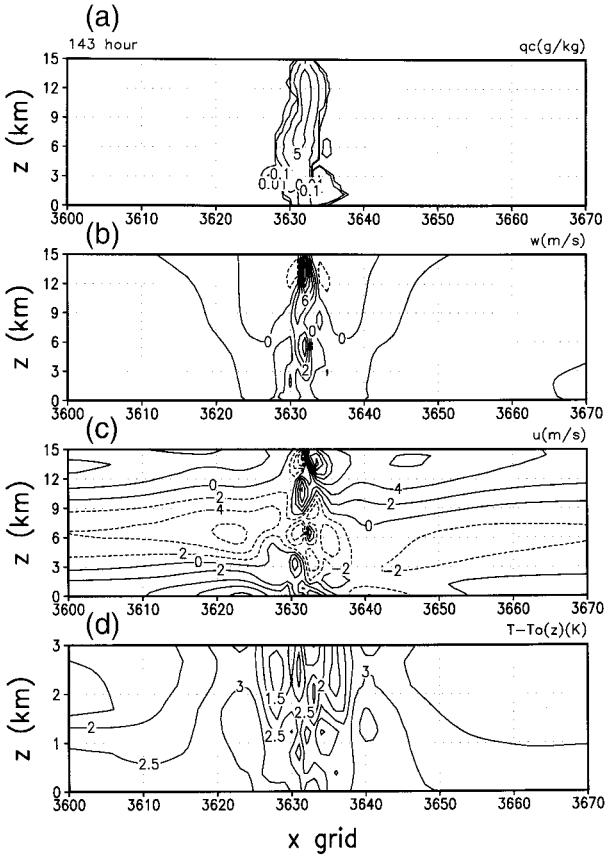

FIG. 7. Cloud structure at hour 143. (a) Cloud content q_c, (b) vertical velocity w, (c) zonal velocity u, and (d) temperature deviation from the initial condition.

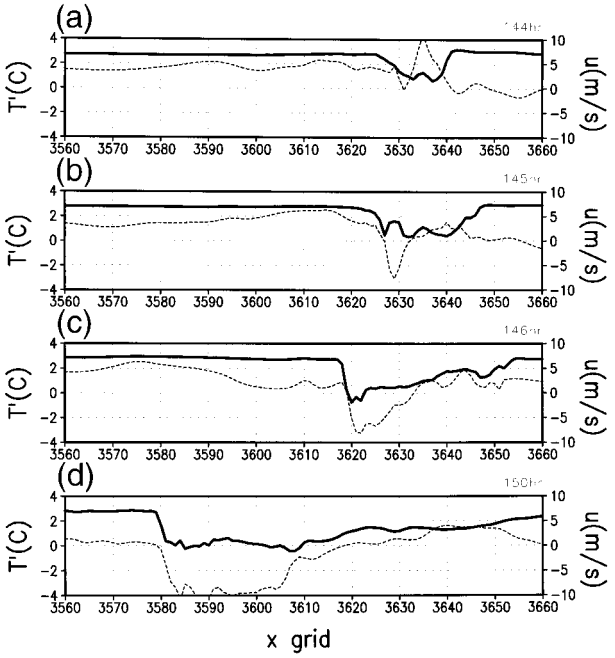

FIG. 8. Temperature deviations from the initial condition at the lowest level (solid) and horizontal winds at 1.33 km (dashed) at (a) hour 144, (b) hour 145, (c) hour 146, and (d) hour 150.

convective activities toward the left edge. By hour 146, the left-edge temperature gradient has been further enhanced by the surface cold-air flow, and the cold-air pool begins to move against the environment flow and carries the convection-regenerating system with it. Within a few hours, a quasi-equilibrium propagating structure is reached, as seen at hour 150 (Fig. 10). The gust front travels steadily westward with 7 m s^{-1} speed. Deep cumulus cells are intermittently generated at and behind it and move rearward (downwind). Some shallow clouds are generated by forward-moving gravity waves in front of the system as seen in Fig. 10 as well as in Fig. 2 (light shaded). If the genesis takes place with winds symmetric to it, for example, in the convergence zone of opposite winds, the process is essentially the same as the above example. The only difference is that the convection will split into two opposite-moving systems as occurred around hour 120, or around hour 336, near the center of the domain. The above analysis indicates that the direction of propagation of the cloud system is initially determined by the low-level background flow during the genesis. It is mostly against the low-level background flow or equivalently, in the direction of the cold-air flow as shown in Fig. 5, unless the background flow is changed later or the cloud system is decaying. In fact, almost all the long-lasting gust front–type cloud systems are propagating against fairly steady low-level background flow. The gust front–type cloud system that develops from a downwind preexistent disturbance generally does not last more than a day if it continues to move downwind. A precipitating convective cloud developed in a calm environment will be short-lived as those clouds over the WP before hour 72.

It is easy to understand that the steadiness of the environmental low-level winds is important to the maintenance of a gust front–type cloud system. Variable winds either in time or in space, especially with magnitude larger than or comparable to the propagation speed of a gust front system, may destroy the system quickly. For example, the short-lived cloud clusters developed around hour 482 over the WP, mentioned in section 4, are in such situations. Shown in Fig. 11 are the surface layer (below 1.33 km) mean wind u, vertical velocity w at 1.33 km, and temperature deviations T' at the lowest grid level (~173 m) of the cloud system between x grids 3210 and 3220 at hours 484, 485, and 486, respectively. In the leftward (negative) flow, the speed increase (from −2 to −8 m s^{-1}) in the front (left) and the speed decrease (from −11 m s^{-1} to near calm) in the rear (right) weaken the temperature gradient and the ascending motion at the gust front and hence lead to the rapid decay of the system. Another example, the vanishing of the two early clusters over the WP between hours 90 and 100 are due to the switch of low-level wind directions over the WP from outward to inward

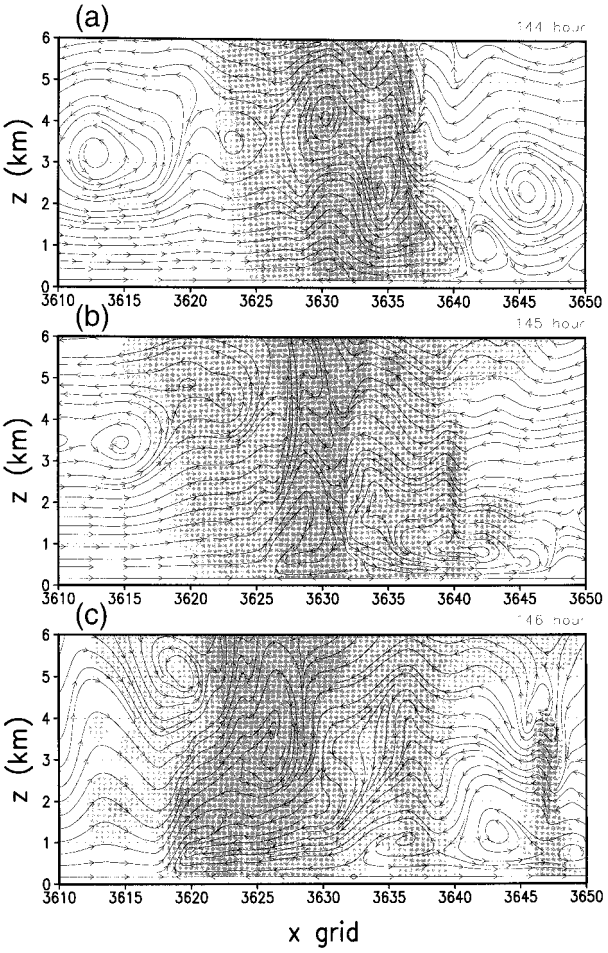

FIG. 9. Streamlines and cloud contents (shaded) at (a) hour 144, (b) hour 145, (c) hour 146. Grades of shade: 0.1, 1, 5 g kg^{-1}.

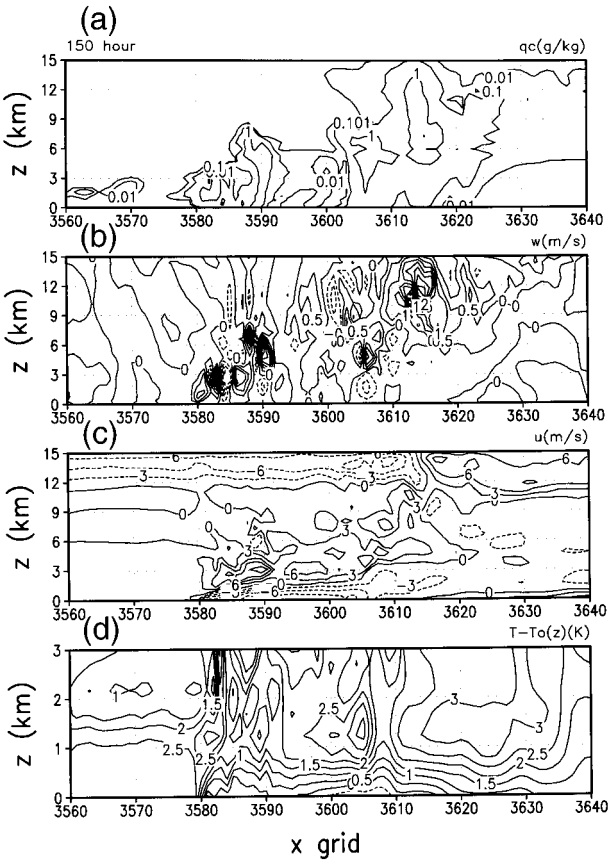

FIG. 10. Cloud structure at hour 150. (a) Cloud content q_c, (b) vertical velocity w, (c) zonal velocity u, and (d) temperature deviation from the initial condition.

with respect to the WP center. Before the switch, the outward winds meet the gust fronts of the incoming cloud clusters head-on, rise above them, and hence support the two cloud clusters. The switch of the wind directions from against to along the gust fronts sharply reduces horizontal mass convergence at the fronts.

Considering the above results, it is not surprising that most gust front–type cloud systems in the experiment are found just outside the model WP, because the area is within the broad convergence zone of the SST-induced flow that favors deep convection and is a region of steady background flow.

When a gust front–type cloud system moving toward the cold water reaches the point beyond which moist convection becomes unfavorable under the cooler environment, the convection weakens and the temperature gradient across the gust front becomes insignificant. It may then vanish as seen around hours 384, 408, and 468, or be driven back by inflow from the lateral boundary as seen around hours 528 and 552.

How are the cloud systems discussed in this section compared with other squall line simulations? Results of

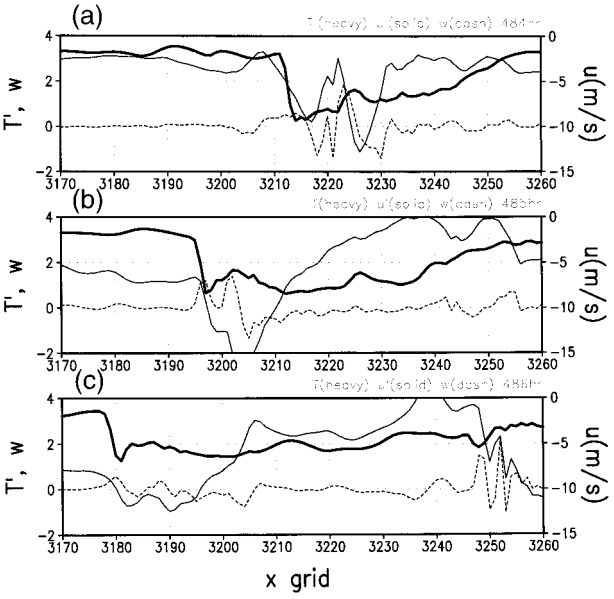

FIG. 11. Surface layer temperature deviation T' (°C, heavy solid), zonal velocity u (m s^{-1}, thin solid), and vertical velocity w (m s^{-1}, thin dashed), at (a) hour 484, (b) hour 485, and (c) hour 486.

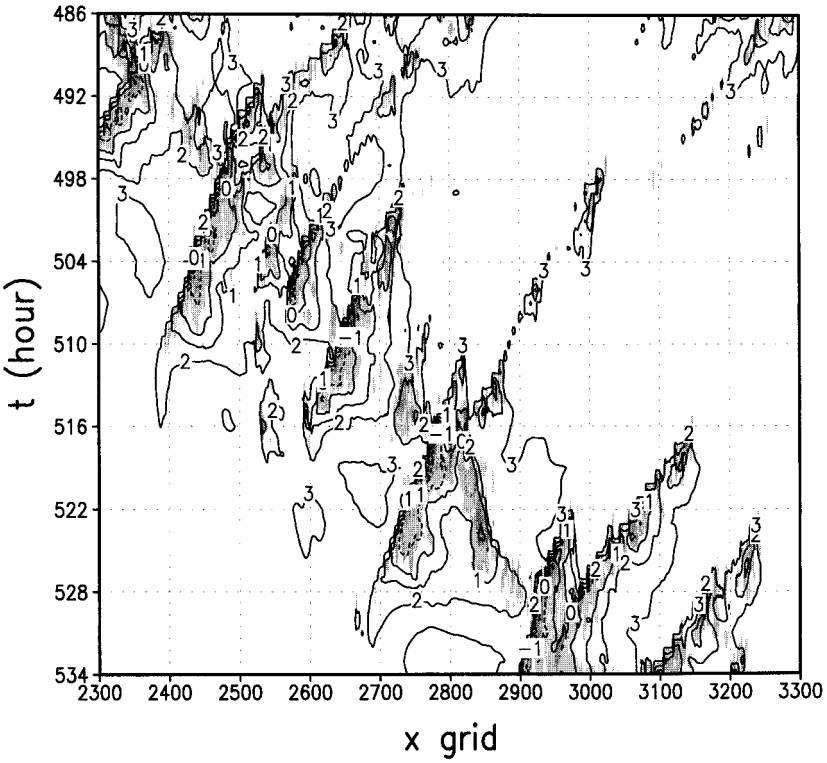

FIG. 12. Temperature deviation from the initial condition at the lowest grid level (contour interval in 1°C) and cloud content (shade grades 0.2 and 1 g kg^{-1}) at 2.23 km.

the two-dimensional simulations of squall lines are sensitive to environment profiles, particularly the wind shear (Nicholls et al. 1988; Fovell and Ogura 1989; Fovell and Dailey 1995). A comparison can be made only if the wind shears are similar. The cloud systems discussed in this section are under environmental low shear $\sim 2 \times 10^{-3}$ s^{-1} below 14 km and reversed shear above. Most of the tropical squall line simulations reported in literature were done focusing on low-level wind shears. Only two adopted wind profiles are grossly similar to the wind profiles in our model. One of Fovell and Dailey's (1995) experiments used a shear 3×10^{-3} s^{-1} below 10 km, no shear above. Their results (Figs. 1e, 2e, and 3e) are in fairly good agreement with ours (Figs. 5d, 5b, and 5c). Note that our temperature field contains zonal average. Yang and Houze (1995) adopted the wind profile of Enid, Oklahoma, for 2331 UTC 10 June 1985, in which the wind increases nonuniformly from -8 m s^{-1} at the surface to 10 m s^{-1} at 10 km, then decreases to 0 and is topped by a jet of 21 m s^{-1} at 14 km. Their results (their Figs. 7a, 8a, 9, and 11) are also in fairly good agreement with our u and w in Fig. 5 and u and w in Fig.6.

6. Cloud systems of higher hierarchy

A more complicated cloud system is found over the WP in the period from hour 462 to hour 582. Figure 12 shows a portion of the time–longitude pattern of the cloud system at the 2.2-km level (shaded). Two characteristic properties are clearly shown. First, the system is made of well-separated clouds that move westward. Second, old clouds disappear at the west while new clouds appear at the east so that the system as a whole propagates eastward. In these aspects, the cloud system resembles the observed SCC reported by Nakazawa (1988) except that here in the model new cumulus clouds emerge at higher frequencies and the westward journeys of the clouds are shorter. Also note that neither the large-scale pattern of the cloud system nor the individual westward propagating substructures travels steadily but pulsates along.

a. Rearward-propagating clouds in the system

The structures of the rearward-propagating clouds in the system are more or less similar to gust front–type cloud systems discussed in section 5. The temperature deviations at the lowest grid level (173m) are plotted in Fig. 12 (contours) together with cloud content (shaded). Clearly, each convective cell in the cloud system is associated with a surface layer colder-air pool. The sharp temperature gradient is on the forward side of the cold pool. Figure 13 shows the x–z sections of a rearward-propagating clusters at hour 522, located in the front of the system and still in the developing stage.

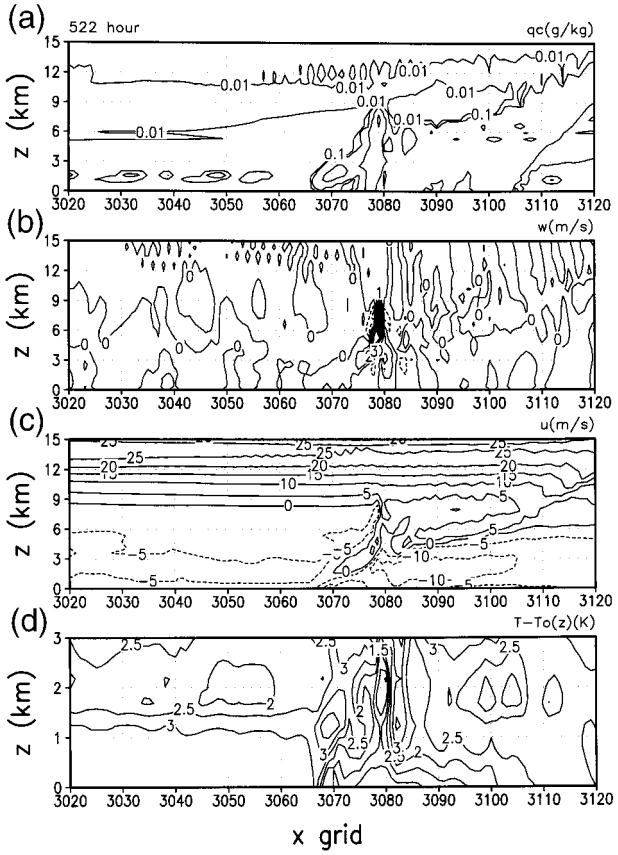

FIG. 13. A substructure in the front (right) of the center at hour 522. (a) Cloud content q_c, (b) vertical velocity w, (c) zonal velocity u, and (d) temperature deviation from the initial condition.

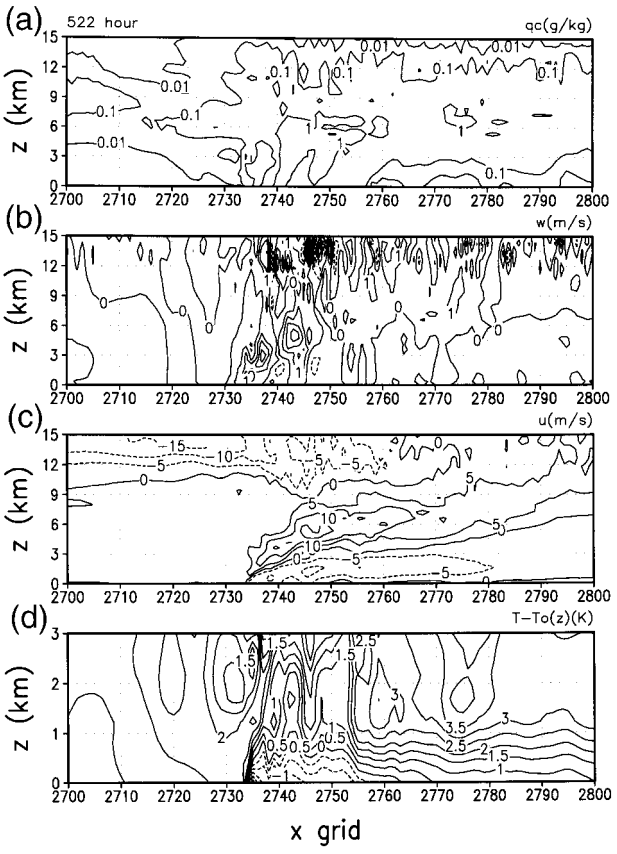

FIG. 14. A substructure in the rear (left) of the center at hour 522. (a) Cloud content q_c, (b) vertical velocity w, (c) zonal velocity u, and (d) temperature deviation from the initial condition.

Seen in Fig. 13 is the 60–70-km-wide and 0.7-km-deep colder-air pool with the sharp temperature gradient on its forward side (Fig. 13d). Stronger cold winds push the gust front toward the left (Fig. 13d) at a traveling speed of 9.3 m s^{-1}. Updrafts and downdrafts are seen above the cold pool just behind the gust front (Fig. 13b). Multiple-cell convective clouds (Fig. 13a) are generated and waves (Fig. 13b) excited above the cold air. Clouds travel backward relative to the gust front. Waves and accompanying shallow clouds are also seen ahead of the gust front in this example. In Fig. 13c, total wind is plotted to show the cold wind as the propagation driver. The strong positive zonal shear seen in Fig. 13c is a part of the flow structure in the front side of the overall system.

Figure 14 shows another gust front–type cloud cluster of the system also at hour 522 but already in the rear. One can see that all things are similar to the one just shown except a negative zonal wind shear in the upper troposphere—a feature of the rear side of the overall system. Figure 15 shows the structure of the convection core at hour 504, consisting of four gust front–type clusters. The second one from the right (front) travels in 7 m s^{-1} speed and the others in 5 m s^{-1} speed. The second one from the left (rear) is decaying. The rightmost one is relatively new. One notices in the third panel the front-side wind shear is opposite to the rear-side wind shear at the upper levels. To sum up, the rearward-moving cloud clusters of the system are of gust front type and their upper-level vertical wind shears over the gust fronts are reversed after crossing the center of the system.

In general, the origins of the rearward-moving cloud clusters can be traced far back in time to some preexisting small perturbations that propagate toward the convective core. This is substantiated in Fig. 16 by the time–longitude distribution of vertical velocity (>5 cm s^{-1}) at the 922-m level. The preexisting small perturbations are shallow-convection cells topped at $\sim$2 km by a stable layer, either brought in from outside by low-level flow or triggered at the front by fast outgoing gravity waves. They develop into deep convective clouds in the front region. Two such examples are shown in Fig. 17. Clouds with q_c of $>10^{-3}$ g kg^{-1} are shaded. Wind speeds are shown by solid (west wind) and dashed (east wind) contours. The four panels from the top down are for hours 515, 516, 522, and 523, respectively. In the time period the center of the system is approximately located

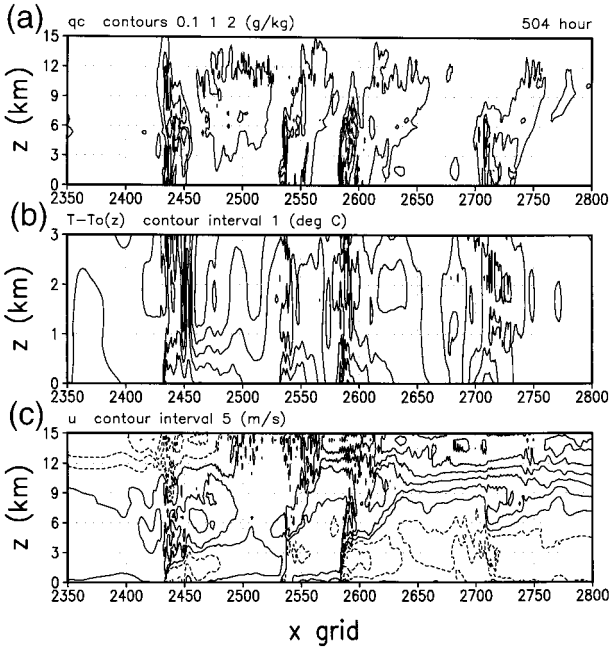

FIG. 15. Structures in the convection core at hour 504. (a) Cloud content q_c, (b) temperature deviation from the initial condition, (c) zonal velocity u.

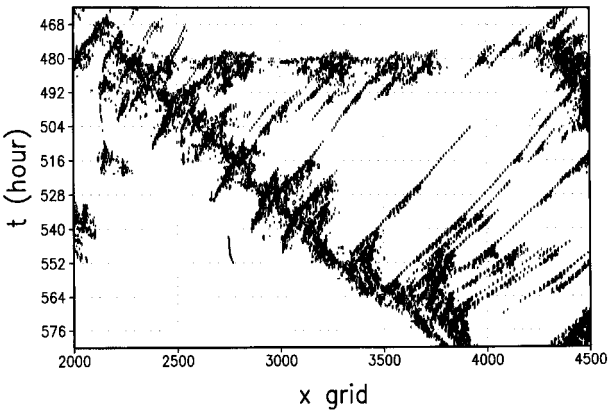

FIG. 16. An x–t diagram of vertical velocity (>5 cm s^{-1}) at 922-m level.

near x grid 2800 and moves eastward. A deep convection develops between hours 515 and 516 from shallow cloud near x grid 3150, about 850 km to the east of the system's center (case D1). Another one develops between hours 522 and 523 near x grid 3240, about 1000 km to the east of the system's center, when the first one, D1, has already well developed and traveled to x grid 3090. The origins of both are traceable to faraway locations (see Fig. 16). Both occurrences take place in a wide easterly flow that is 5 to 6 km deep. No flow comes from the system's center side before or during each occurrence. They are, therefore, not the outcome of the tele-induction mechanism described in CL (see Figs. 2, 3 in CL for comparison).

To understand how and why the boundary layer shallow clouds grow into deep cumuli, take D1 for example. Figure 18 displays some sequential snapshots of q_c and w associated with D1 (in uneven time intervals). Notice that in front of the SCC-like cloud system there are gravity waves propagating outward from the convection core with noticeable outward spectral redshift as a result of dispersion. Case D1, which is a surface layer dry disturbance at hour 508 identifiable as a residual from previous convection (see Figs. 12 and 16), starts again to produce shallow clouds in hour 510. But the clouds remain shallow for the next 5 to 6 h. Figure 19 shows that the clouds remain shallow because the convection is capped by a stable layer around 800 hPa during this time period. Deep convective cloud starts to appear at hour 516 (as seen in Fig. 17e) only when the static stability of the cloud-top layer around 800 hPa becomes marginal to moist ascent (the leftmost sounding in Fig. 19). The removal of the capping is achieved by gradual temperature decrease above the clouds. The temperatures below the cloud remain almost unchanged, as clearly shown in Fig. 19.

What mechanisms are responsible for the temperature decreases in the deep layer above the shallow convection? There are adiabatic cooling and heating accompanying the passing waves shown in Fig. 18. Do they contribute to the removal of the convection-capping stable layer, and how important is it? The passing gravity waves are apparently weak. The adiabatic cooling caused by any of them is not strong enough to remove the capping stable layer nor can the waves lift the con-

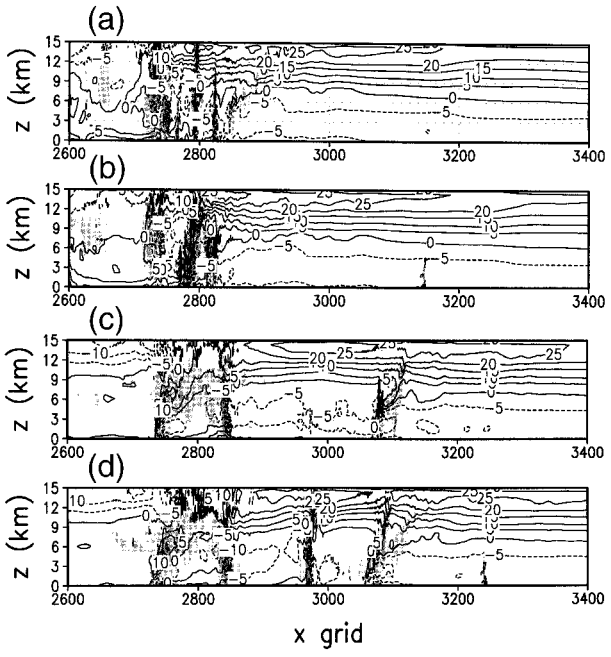

FIG. 17. The u (contour interval 5 m s^{-1}) and cloud content q_c (>1 g kg^{-1} shaded) at (a) hour 515, (b) hour 516, (c) hour 522, and (d) hour 523.

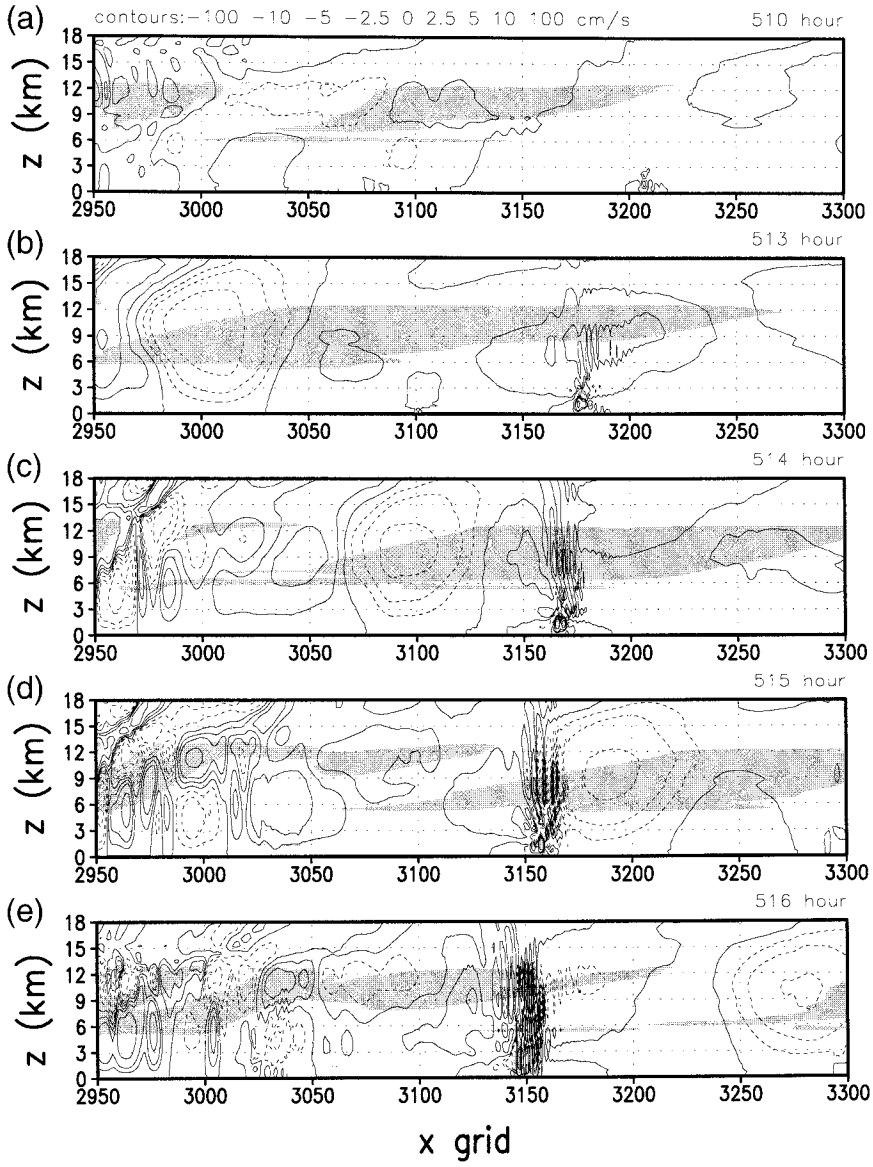

FIG. 18. Vertical cross sections of cloud content (grades of shade: 0.01, 0.1, 1) and vertical velocity (cm s^{-1}) associated with D1 at (a) hour 510, (b) hour 513, (c) hour 514, (d) hour 515, and (e) hour 516.

vection through it until it is about to lose its grip after weakening. Figure 20 shows the time–longitude pattern of temperature deviation (from the initial condition) at the 4.3-km level from hour 510 to hour 517. It is qualitatively representative in the deep layer between the capped cloud and the 400-hPa level. Evidently, beside the temperature oscillations corresponding to the passing gravity waves, the whole region is apparently under cooling from the beginning to the end of the time period. In this period, the capped shallow convection travels from grid 3207 to grid 3147 and can be traced in Fig. 20 via the fast but weak temperature changes caused by the localized small oscillations at the cloud (see Fig. 18). Along its track, the temperature at this level first oscillates slightly within one-quarter of a degree celsius, then drops about one degree, rises again about half a degree, then drops again about a seventh of a degree. The accumulated total temperature drop in the time period is 1.25 degree celsius along the track, almost equally due to the apparently non-oscillatory temperature decrease and the last larger-amplitude oscillation.

The apparently non-oscillatory temperature decrease above the shallow convection can be accounted for as follows: In the core of the SCC-like system, a surface cooling layer and an upper-level warming layer are maintained. The latter descends while extending outward from the core region. In the front region, the lowering of the warming layer is usually overshadowed by

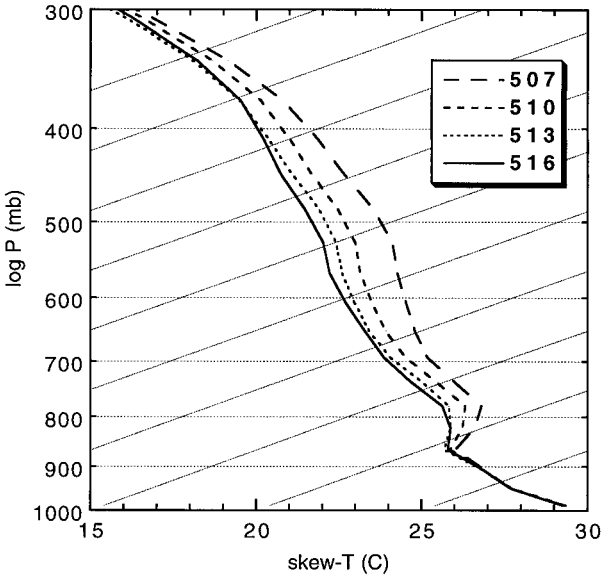

FIG. 19. Skew-*T* diagram of temperature over the perturbation D1.

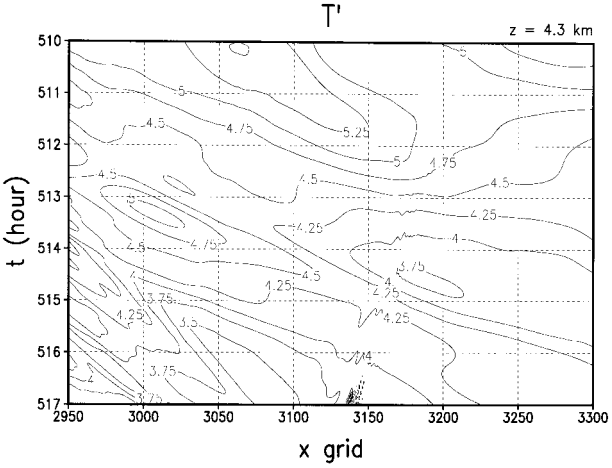

FIG. 20. An *x*–*t* diagram of temperature deviation (contour interval 0.25°C) at the 4.3-km level.

stronger oscillations associated with short gravity waves as shown in Fig. 20. It is clear seen in Fig. 21 that shows the temperature departure (from the initial condition) at hour 508 just before D1 starts. Notice that due to the outward lowering of the warm layer, temperature decreases inward from grid 3370 to grid 3100 (about 600 km from the deep-convection core) in the deep layer between 2 and 8 km. This thermal structure is moving rightward causing the local cooling in the layer as shown in Fig. 20 while the shallow convection drifts leftward with the boundary layer flow from grid 3237 at hour 508 to grid 3137 at hour 517. Not counting the passing oscillations, the shallow convection enters into a cooler

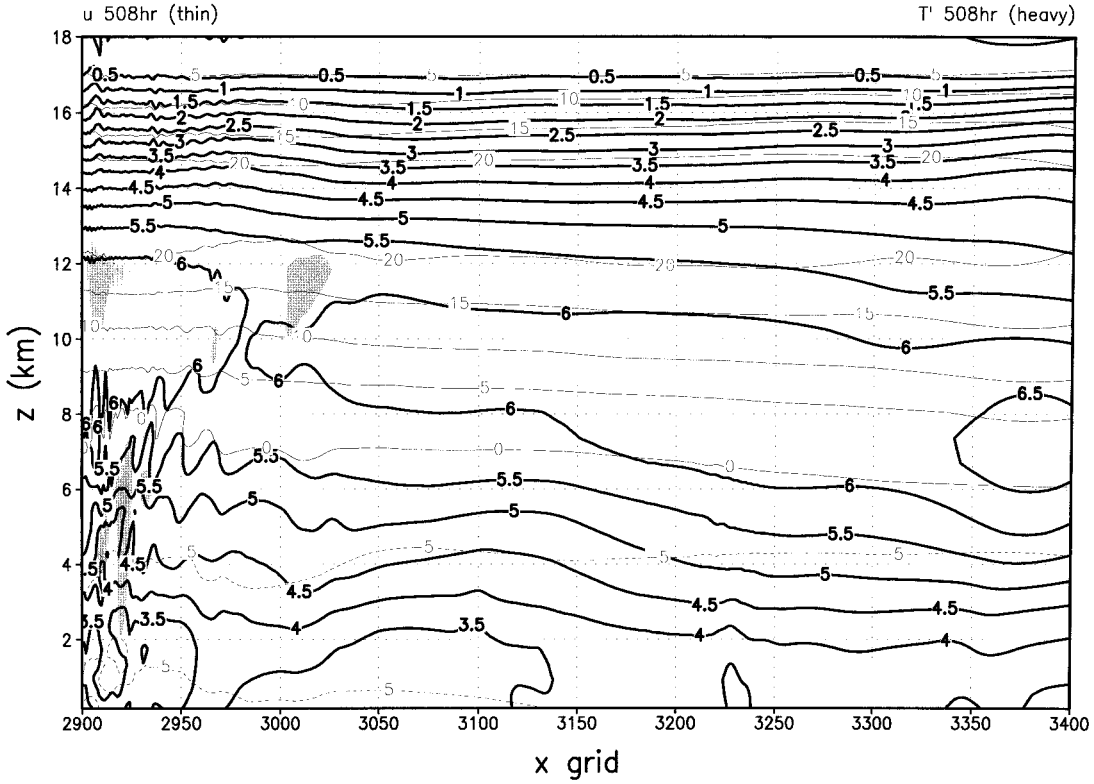

FIG. 21. An *x*–*z* distribution of the temperature deviation from the initial condition (contour interval 0.5°C), zonal wind (contour interval 5 m s^{-1}), and cloud content (grades of shade: 0.1, 1) at hour 508.

and cooler environment between 2 and 8 km with a steady temperature drop slightly more than a half degree to make the cloud-top layer near moist adiabatic.

The mechanism responsible for outward moving and lowering of the warming layer outside the core region is essentially explained by the theoretical studies of gravity waves forced by a top-heavy heating profile in an atmosphere at rest (Nicholls et al. 1991; Pandya et al. 1993; Mapes 1993). It is basically due to the dispersive separation of the first two vertical gravity modes excited by the heating [see Fig. 5b in Nicholls et al. (1991) and Fig. 5 in Mapes (1993)]. Only the situation here is more complicated because, not as assumed in those studies, the atmosphere is not at rest but with vertical shear and the internal heating is neither fixed in a single column nor of a simple shape. So here we have multiple oscillatory internal heat sources, each excites gravity modes that interfere with those from other sources and each wave structure is necessarily asymmetric about the source and more or less tilted by the vertical shear. Nevertheless, it is expected that the frontmost deep convection will have the most influence on things farther outward from there. The farther out, the lesser interference from the others. Therefore, the mechanism of spectral separation found in those simple theoretical cases may still apply except that the transition in spectral separation is less abrupt. In fact, the lowering of the warming layer outside the core region can be seen in the composite structure of temperature perturbation shown in Fig. 22c. The excessive interference from other deep oscillatory heating near the frontmost convection is likely the reason why new deep convection does not develop closer to the existing one than it does.

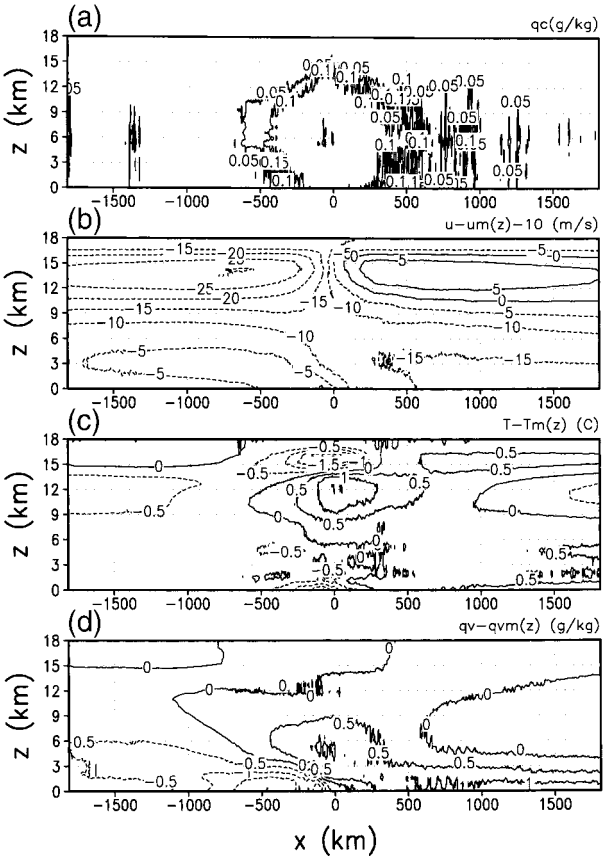

FIG. 22. Time composite of the SCC-like structure using the convection center as reference. (a) Cloud content (contours: 0.05, 0.1, and 1 g kg^{-1}), (b) perturbation horizontal velocity relative to the moving center, (c) perturbation temperature, and (d) perturbation specific humidity.

b. A composite of the system

To estimate the average structure of the SCC-like convective cloud system, composites over two domain sizes are obtained using the traveling center as the reference point. The wider composite domain, indicated by the wider quadrangle in Fig. 3, includes 725 grid points on each side of the traveling center and covers 60 h in time. To exclude the cloud systems wandering near the warm water edges, the domain of composite cannot be wider. The narrower domain, indicated by the narrower quadrangle in Fig. 3, includes only 120 grid points on each side, representing the convective core, but covers longer sampling time interval, 90 h. The results obtained for the narrower domain are not significantly different from the correspondent part of the results obtained for the wider domain and therefore will not be shown separately. One must bear in mind, however, that the composite procedure necessarily smoothens all relatively moving substructures and therefore leaves only a simplistic view of the overall system.

Except the composite of cloud content, each composite field obtained with the wider domain is separated into two parts: the quantity averaged over the x direction, to be called the zonal average, and the remainder of the composite field after removing the zonal average, to be called the perturbation field. Figure 22 shows the composite fields of cloud content (q_c), the perturbation zonal wind relative to the moving center ($u' - c$), the perturbation temperature (T'), and the perturbation specific humidity ($q_{v'}$); and Fig. 23 shows the accompanying zonal averages. The magnitudes and depths of the three zonal shear layers and the vertical profile of zonal temperature increase agree well with those shown in Fig. 4b and Fig. 4d, respectively. We also note that on the traveling path of the system, zonally averaged winds at all levels are significantly smaller than the propagating speed of the system (10 m s^{-1}); hence the system is not steered by the zonally averaged flow.

Figure 22a shows the total specific mixing ratio of condensed water in the cloud. The contour lines are 0.05, 0.1, and 1×10^{-3} g kg^{-1}. The cloud content is rather low compared with an individual cloud, reflecting the fact that at a given spot in the system, including the center, cloud exists only for a fraction of the time. The area of intermittent cumulus clouds extends about 1400

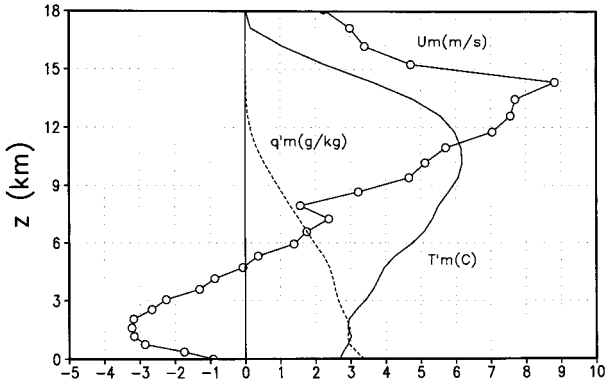

FIG. 23. Zonal averages of the composite over the 1451-gridpoint domain. Horizontal velocity u_m, temperature deviation T'_m, and specific humidity deviation q'_m.

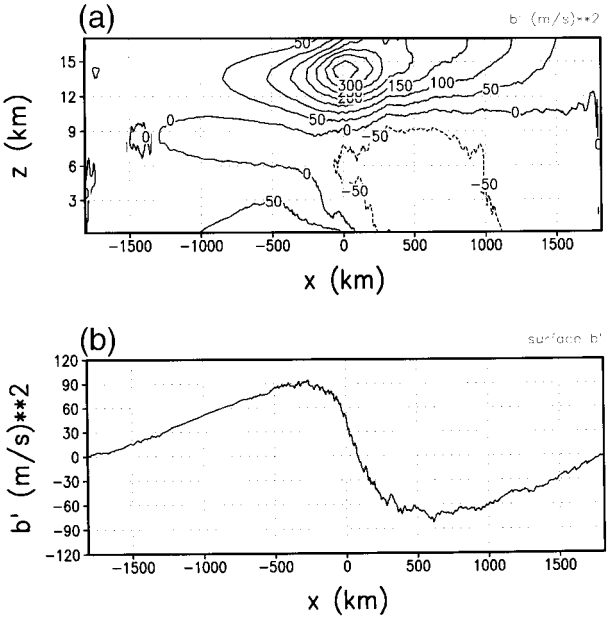

FIG. 24. Perturbation pressure function b' ($\equiv\rho_0^{-1}p'$), (a) as a function of x and z, and (b) at the surface as a function of x.

km ahead of the center, but only about 700 km behind the center.

The relative perturbation wind field ($u' - c$, Fig. 22b) shows that a deep layer of flow, from the surface up to 11 km, comes in from the front, sharply converges within about 400 km around the center, and exits from the rear. In the layer above 11 km, the flow diverges outward sharply over the core area, most to the rear, while only a small portion back to the front. The maximum outflow exists just below the 14-km level and about 700 km behind the center. The maximum inflow is at the top of the boundary layer but located farther out to the front.

Returning to earth-relative flow field by adding 10 m s^{-1} (the propagation speed) back to Fig. 22b, however, the airflows above 7 or 8 km are always outward with respect to the convection center and those below 7 or 8 km are almost all inward except in a small area close to the center where the front surface layer flow is outward. Since the center travels faster than the rear inflow, the air in the rear inflow does not enter from the rear but actually comes from the front. This is important to the understanding of the dryness of the rear inflow to be described later. Why is the air from the front turning frontward after passing the center? The turnabout is forced by the frontward pressure force around the center (see Fig. 24a). The front inflow begins slowing down when the center is about 500 km away and approaching. It turns back frontward about the time when the center passes. The turning back occurs along the -10 m s^{-1} contour behind the center shown in Fig. 22b. After the turning back the air moves toward the center but lags farther and farther behind.

The temperature perturbation (Fig. 22c) shows a positive region in the convective core sandwiched between a negative region below 6 km and another smaller negative region above 14 km. Consistent with the zonal average shear (Fig. 23), the middle positive region shifts toward the front while the top and bottom negative regions shift rearward. This distribution generates an asymmetric mass distribution about the center. The positive perturbation covers the convective core from about 5 to 14 km where the released latent heat is in excess of adiabatic cooling, and extends outward along the front outflow. The surface negative region, centered at 150 km in the rear, is concentrated in the subcloud layer from 120 km in the front to 400 km in the rear. The cooling is mainly due to the evaporation of raindrops. The top negative region, centered at 15.5 km, is due to the forced ascending along the upward perturbation pressure gradient (see Fig. 24a).

From the inside of the convective core (within about 600 km from the center) to the front region, the vertical distribution of temperature perturbation gets reversed. Outside the core, the axis of positive perturbation temperature descends to the lower layer. Combining it with the zonal average in Fig. 23, will generally recover the type of thermal structure shown in Fig. 21. Recall in the above section that such thermal structure can be explained by thermally forced gravity waves and is important to the development of deep convection in the front region. The perturbation thermal structure suggests that the overall composite of the SCC-like system is basically an internally heated mode-1 gravity wave with thermal structure horizontally shifted in the direction of the deep zonally averaged wind shear.

The perturbation specific humidity is shown in Fig. 22d. If the normal rapid vertical decrease of humidity were adequately taken into account—for instance, if the perturbation were expressed in percentage of the initial value—the pattern of the perturbation specific humidity would be very much similar to that of the temperature perturbation. Even in the present form, they are grossly alike. One might contribute this similarity to the tem-

perature dependence of saturation humidity, but it is more than that. The boomerang-shaped positive region generally follows the central path of the front inflow–outflow circulation. The front high surface value is due to the accumulation of moisture flux from the sea surface. The positive value in the convective core is brought by the rising of surface layer moisture-rich inflow. The reason for the large low-level moist deficit behind the center is simply that the air in the rear inflow is from the front, as pointed out earlier, and has been dried by precipitation in the convective core. The sea surface moisture flux only gradually reduces the moisture deficit. The transition from humid in the front to dry in the rear enhances the mass asymmetry about the center.

Figure 24 shows the composite perturbation pressure field after the removal of the zonally averaged pressure gradient. Above 10 km, the pressure perturbation field has a strong symmetric component about the center. From 9 km down it becomes more and more antisymmetric, consistent with the asymmetric mass distribution created by the temperature and humidity perturbations. At the surface, the field becomes completely antisymmetric with a low pressure in the front and a high pressure in the rear, favoring forward propagation. As noted earlier, the perturbation pressure gradients below the 9-km level around the center are responsible for turning the low-level incoming rearward flow to lagging frontward flow during the center's passage.

The above results of the composite present the following self-consistent picture: The overall convection system, basically a gravity wave of mode 1 with asymmetric pressure perturbation as shown in Fig. 24a, travels 10 m s^{-1} eastward in the vertically sheared zonal flow shown in Fig. 23. Its low-level front inflow is decelerated by the eastward pressure force within 500 km from the center, hence converges, rises, and rains around the center. Most of the air, now drier and with much less CAPE, is left forever behind. Only a portion of the air that has reached the upper troposphere is accelerated eastward by the perturbation pressure force. During the process, significant warming occurs in the middle and upper troposphere where the released latent energy is in excess and significant cooling occurs at the lower levels where evaporation takes place on falling raindrops. The resulted temperature perturbations and similar humidity perturbations, with their centers horizontally shifted in the direction of the zonal averaged shear, create the mass distribution, with moisture-rich and warmer air in the front and drier and cooler air in the rear, which maintains the perturbation pressure field of the system and continues to move the system forward. In short, the overall system is basically a mode-1 gravity wave with an internal heat source moving in the direction of zonally averaged main (deep) wind shear.

c. A comparison of two cloud systems

It is interesting to compare the SCC-like system with the cloud system over the WP in the period between hours 366 and 438, propagating westward with a speed of about 13 m s^{-1} (see Fig. 3). Beside traveling in opposite directions, the two systems have significantly different substructures as evident in Fig. 3. Particularly noticeable is the horizontal expansion of the west-going system after hour 390. It is related to the vanishing of the left-side cluster at hour 385. The low-level inflow from the left-side lateral boundary cannot directly reach the system before hour 385 due to the blockage of the left-side cluster.

As above, composite fields are obtained between hours 378 and 426 with a 1451 gridpoint domain centered at the traveling center of the system. Each composite field is again separated into zonal average and perturbation. The zonal averages and perturbation fields (not shown) show that the patterns of all the perturbation fields and the vertical profile of zonally averaged wind are generally the mirror images of those in Fig. 22 and Fig. 23, respectively. The vertical profiles of zonal averages of temperature and humidity departures are quite similar to those in Fig. 23, respectively. In other words, the scalar quantities are similar and the vector quantities (zonally averaged winds and perturbation fields) are generally symmetric with respect to the direction of propagation. This indicates that the overall dynamics of the two cloud systems are the same. However, their differences in substructures indicate that *the substructures are not entirely controlled by the intrinsic dynamics but subject to external interference.* The fact that the vector quantities in the two sets of composites are respective mirror images also give us some assurance that the composites are not contaminated in the composite-making process by the nonuniform stationary system shown in Fig. 4.

7. Summary and discussion

A two-dimensional cloud ensemble model is integrated over a basin-scale domain with prescribed warm-pool type SST distribution, to study the formation and evolution of cloud clusters over a large-scale warm pool. The initial atmosphere is at rest with zonally uniform thermodynamic properties. The vertical profiles of temperature and humidity are the averaged values over the TOGA region over the periods when convective activities are relatively subdued. After about 10 days of spin-up to compromise the dis-equilibrium between the imposed SST gradient and the initial zonally uniform atmosphere, a quasi-stationary twin-cell Walker-type circulation is built up as background flow and to interact with the mesoscale deep convection. Over the area of uniform warm SST where the Walker-type circulation is relatively weaker, the interaction is more effective and becomes the primary source of the model's multiscale variability and organization. One of the interesting results is that zonal wind shears are generated across the warm pool in company with the propagating large-scale cloud system.

Most deep convective clouds in the model appear organized in hierarchical clustered patterns and are limited to the area of warm SST above 28°C (Fig. 3). The most fundamental cloud cluster in the model has a horizontal scale of a few hundred kilometers. It is of gust front type, meaning that new cumulus clouds in the cluster are generated at the leading edge of a propagating surface cold-air pool—the ''gust front.'' The genesis of the gust front–type cloud cluster is most favorably initiated by an intensive deep convection in a background shear flow. The quasi-stationary slowly varying wind systems provided by the imposed SST environment enable the cloud clusters to persistently thrive as seen in Fig. 3.

Large hierarchical propagating cloud systems in the model have horizontal scales up to 3000 km and consist of up to four cloud clusters that are generally of gust front type. The constituent cloud clusters are generated intermittently and have life spans of 12–36 h. The collection of the top-heavy internal heating associated with the constituent cloud clusters induces an overall troposphere-deep dynamic (gravity) wave. The overall wave travels in the direction of the tropospheric deep shear at a speed determined by the thermodynamic asymmetry in the wave as revealed by the moving composites. Warm and moist air comes into the system at the front end and dumps water in the convective core. The middle, and major, portion of the air continues its rearward journey; the upper portion turns back in front of the center, gradually subsiding and rejoining the incoming flow later; the lowest portion also turns back but lags forever behind the center. Such a flow structure creates a cooler and much drier atmosphere in the rear as compared to the atmosphere in the front. The asymmetric mass evolution in turn results in a rear-increasing and front-decreasing pressure perturbation. This pressure asymmetry supports the propagation of the overall wave.

Due to the combined effect of subsidence in the overall wave and the gravity modes excited by the constituent cloud clusters on low-tropospheric stability, the development of new deep cumuli are generally favored somewhere in the front region, unless outside influence becomes important. In the case where the inflow at the front end of the hierarchical cloud system is steady, except for containing weak small-scale boundary layer disturbances, for example, between hours 492 and 552, deep cumulus cloud clusters develop intermittently from shallow disturbances hundreds of kilometers ahead of the nearest deep convection in the system. The hierarchical cloud pattern structurally resembles the observed equatorial super cloud cluster (SCC) in the time–longitude plot. However, the life spans of the constituent cloud clusters here are shorter than that in the observed SCC.

The shorter life span of the constituent cloud clusters may be partly attributable to the adopted initial static stability profile that characterizes subdued convective activities. It may be argued that, if a less stable profile were adopted, new deep convection would develop earlier and farther out than, for instance, D1 did (section 6a), and the cloud cluster developed from D1 would be more vigorous and last longer. To stretch the argument further, the frequent, weaker new clusters might then be replaced by less frequent, more vigorous new clusters.

The unrealistic aspects of our experiment are 2D limitation and allowing no SST response to boundary forcing. Both will undoubtedly affect the details of the result. But the basic characteristics of the results should still hold. Still another unrealistic aspect is the exclusion of the effects of the earth's rotation, due to the two-dimensional nature, which makes the dynamics of the east- and west-moving modes indistinguishable and definitely affects the east–west structure of the large-scale clusters. Allowing the effect of the earth's rotation in the model dynamics would suppress the splitting of a large convective cluster into two opposite propagating equals. The lacks of cloud–radiation interaction, diurnal variation, and large-scale perturbations certainly have made the results much simpler. The sharp change in the prescribed SST gradient may have exaggerated the SST effect. The open boundary condition cannot adequately take into account the outside responses. Despite all these unrealistic aspects, our model results suggest that the environment conditions provided by the Pacific warm pool positively contribute to the formation and the maintenance of the cloud cluster hierarchy in the region. This work only represents a preliminary approach to a very complex problem. The removal of the unrealistic aspects of experimental design awaits more, future, work. To test how much the main results depend on the specific SST distribution, further testing with more realistic SST is also desirable.

Acknowledgments. We wish to thank Dr. Brian E. Mapes for his reviews of the earlier versions of the manuscript and his suggestions, particularly on interpreting the model results, with which major improvements were made. This research is supported under the Tropical Rainfall Measuring Mission of NASA's Mission to Planet Earth Office.

REFERENCES

Bannon, P. R., 1995: Potential vorticity conservation, hydrostatic adjustment and the anelastic approximation. *J. Atmos. Sci.,* **52,** 2302–2312.

Chao, W. C., and S.-J. Lin, 1994: Tropical intraseasonal oscillation, super cloud clusters, and cumulus convection schemes. *J. Atmos. Sci.,* **51,** 1282–1297.

——, and L. Deng, 1998: Tropical oscillation, super cloud clusters, and cumulus convection schemes. Part II: 3D aqua-planet simulation. *J. Atmos. Sci.,* **55,** 690–709.

Chen, C., 1995: Numerical simulations of gravity currents in uniform shear flows. *Mon. Wea. Rev.,* **123,** 3240–3253.

Chen, S. S., and R. A. Houze Jr., 1996: Multiscale variability of deep convection in relation to large-scale circulation in TOGA COARE. *J. Atmos. Sci.,* **53,** 1380–1409.

Deardorff, J. W., 1975: The development of boundary-layer turbulence models for use in studying the severe storm environment. *Proc. SESAME Opening Meeting*, Boulder, CO, NOAA/ERL, 251–264.

Fovell, R. G., and Y. Ogura, 1988: Numerical simulation of a midlatitude squall line in two dimensions. *J. Atmos. Sci.,* **45,** 3846–3879.

——, and ——, 1989: Effect of vertical shear on numerically simulated multicell storm structure. *J. Atmos. Sci.,* **46,** 3144–3176.

——, and P. S. Dailey, 1995: The temporal behavior of numerically simulated multicell-type storms. Part I: Modes of behavior. *J. Atmos. Sci.,* **52,** 2073–2095.

Klemp, J. B., and R. B. Wilhelmson, 1978: The simulation of three-dimensional convective storm dynamics. *J. Atmos. Sci.,* **35,** 1070–1096.

Kuma, K., 1994: The Madden and Julian oscillation and tropical disturbances in an aqua-planet version of JMA global model with T63 and T159 resolution. *J. Meteor. Soc. Japan,* **72,** 147–172.

Lau, K.-M., L. Peng, C.-H. Sui, and T. Nakazawa, 1989: Dynamics of super cloud clusters, westerly wind burst, 30–60 day oscillation, and ENSO: A unified view. *J. Meteor. Soc. Japan,* **67,** 205–219.

——, T. Nakazawa, and C.-H. Sui, 1991: Observations of cloud cluster hierarchies over the tropical western Pacific. *J. Geophys. Res.,* **96,** 3197–3208.

Lin, Y.-L., R. D. Farley, and H. D. Orville, 1983: Bulk parameterization of the snow field in a cloud model. *J. Climate Appl. Meteor.,* **22,** 1065–1092.

——, R. L. Deal, and M. S. Kulie, 1998: Mechanisms of cell regeneration, development and propagation within a two-dimensional multicell storm. *J. Atmos. Sci.,* **55,** 1867–1886.

Lipps, F. B., 1990: On the anelastic approximation for deep convection. *J. Atmos. Sci.,* **47,** 1794–1798.

Liu, C., and M. W. Moncrieff, 1996: A numerical study of the effects of ambient flow and shear on density currents. *Mon. Wea. Rev.,* **124,** 2282–2303.

Mapes, B. E., 1993: Gregarious tropical convection. *J. Atmos. Sci.,* **50,** 2026–2037.

——, and R. A. Houze Jr., 1993: Cloud clusters and superclusters over the oceanic warm pool. *Mon. Wea. Rev.,* **121,** 1398–1415.

Moncrieff, M. W., 1989: Analytical models of narrow cold-frontal rainbands and related phenomena. *J. Atmos. Sci.,* **46,** 150–162.

——, and M. J. Miller, 1976: The dynamics and simulation of tropical cumulonimbus and squall lines. *Quart. J. Roy. Meteor. Soc.,* **102,** 373–394.

——, and C. Liu, 1999: Convection initiation by density currents: Role of convergence, shear, and dynamical organization. *Mon. Wea. Rev.,* **127,** 2455–2464.

Nakajima, N., and T. Matsuno, 1988: Numerical experiments concerning the origin of cloud clusters in the tropical atmosphere. *J. Meteor. Soc. Japan,* **66,** 309–329.

Nakazawa, T., 1988: Tropical super clusters within intraseasonal variation over the western Pacific. *J. Meteor. Soc. Japan,* **66,** 823–839.

Nicholls, M. E., R. H. Johnson, and W. R. Cotton, 1988: The sensitivity of two-dimensional simulations of tropical squall lines to enviromental profiles. *J. Atmos. Sci.,* **45,** 3625–3649.

——, R. A. Pielke, and W. R. Cotton, 1991: Thermally forced gravity waves in an atmosphere at rest. *J. Atmos. Sci.,* **48,** 1869–1884.

Numaguti, A., and Y.-Y. Hayashi, 1991: Behavior of cumulus activity and the structures of circulations in an ''aqua planet'' model. Part I. The structure of the super cloud clusters. *J. Meteor. Soc. Japan,* **69,** 541–561.

Oohchi, K., 1999: Hierarchical organization of super cloud cluster caused by WISHE, convectively induced gravity waves and cold pool. *J. Meteor. Soc. Japan,* **77,** 907–927.

Pandya, R., D. Durran, and C. Bretherton, 1993: Comments on ''Thermally forced gravity waves in an atmosphere at rest.'' *J. Atmos. Sci.,* **50,** 4097–4101.

Rotunno, R., J. B. Klemp, and M. L. Weisman, 1988: A theory to strong, long-lived squall lines. *J. Atmos. Sci.,* **45,** 463–485.

Soong, S.-T., and Y. Ogura, 1980: Response of trade wind cumuli to large-scale processes. *J. Atmos. Sci.,* **37,** 2035–2050.

——, and W.-K. Tao, 1980: Response of deep tropical clouds to large-scale processes. *J. Atmos. Sci.,* **37,** 2016–2036.

Sui, C.-H., and K.-M. Lau, 1992: Multiscale phenomena in the tropical atmosphere over the western Pacific. *Mon. Wea. Rev.,* **120,** 407–430.

Tao, W.-K., 1983: A numerical study of the structure and vertical transport properties of a convective system. Ph.D. dissertation, University of Illinois, 228 pp.

——, and S.-T. Soong, 1986: A study of the response of deep tropical clouds to mesoscale processes: Three-dimensional numerical experiments. *J. Atmos. Sci.,* **43,** 2653–2676.

——, and J. Simpson, 1993: Goddard cumulus ensemble model. Part I: Model description. *TAO,* **4,** 35–72.

——, ——, and M. McCumber, 1989: An ice-water saturation adjustment. *Mon. Wea. Rev.,* **117,** 231–235.

Xu, Q., and M. W. Moncrieff, 1994: Density current circulations in shear flows. *J. Atmos. Sci.,* **51,** 434–446.

Xue, M., Q. Xu, and K. E. Droegemeier, 1997: A theoretical and numerical study of density currents in nonconstant shear flows. *J. Atmos. Sci.,* **54,** 1998–2019.

Yang, M.-J., and R. A. Houze Jr., 1995: Multicell squall line structure as a manifestation of vertically trapped gravity waves. *Mon. Wea. Rev.,* **123,** 641–660.

Yano, J.-I., and N. Nishi, 1989: The hierarchy and self-affinity of the time variability within the tropical atmosphere inferred from the NOAA OLR data. *J. Meteor. Soc. Japan,* **67,** 771–788.

——, J. C. McWilliams, M. W. Moncrieff, and K. A. Emanuel, 1995: Hierarchical tropical cloud systems in an analog shallow-water model. *J. Atmos. Sci.,* **52,** 1723–1742.